# Large and stable reversible lithium-ion storages from mesoporous SnO$_2$ nanosheets with ultralong lifespan over 1000 cycles

Xiao Zhang, Bin Jiang, Jinxue Guo[*], Yaping Xie, Lin Tang

*Key Laboratory of Science Analysis of Tumor Marker (Ministry of Education), College of Chemistry and Molecular Engineering, Qingdao University of Science and Technology, Qingdao 266042, China*
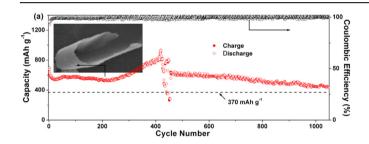
## HIGHLIGHTS

- Mesoporous SnO$_2$ NSs are synthesized via EISA followed by calcination.
- Large surface area and high pore volume of SnO$_2$ NSs are induced by porous features.
- SnO$_2$ NSs exhibit excellent capacity retention ability with high reversible capacity.
- Cycle life of pure SnO$_2$ NSs has been extended as long as 1000 cycles.
- Stable 2D sheet-like structure is the major reason for its outstanding durability.

## GRAPHICAL ABSTRACT

## ABSTRACT

The major challenge to promote the commercialization of SnO$_2$ anode materials is to construct unique structures and/or composites that could alleviate the volume effect and extend the lifespan. This study develops an efficient synthetic solution for the preparation of mesoporous SnO$_2$ nanosheets, which involves an evaporation-induced selfassembly process and the following thermal treatment. Surfactant F127 is used as the soft template to form abundant cores. The as-prepared sample intrinsically inherits flexible sheet-like structure and porous features, as characterized with XRD, SEM, TEM and BET techniques. Based on these combining structural benefits, the sample is utilized as anode materials for lithium-ion batteries and exhibits excellent Li$^+$ storage performance such as large and stable reversible capacity, good rate capability, and especially the outstanding durable cycling life of over 1000 cycles, which meets the demands of practical applications. The structural changes of SnO$_2$ nanosheets are observed from the decomposed electrodes after different electrochemical cycles. Moreover, this synthesis strategy may offer an alternative and universal approach for synthesis of other transitional metal oxides or their binary composites as high-performance anode materials for lithium-ion batteries.

© 2014 Elsevier B.V. All rights reserved.

## 1. Introduction

Recently, SnO$_2$ has been investigated intensively as next generation high-performance lithium-ion batteries (LIBs) anode materials due to its numerous appealing features, including natural abundance, low cost, environmental friendliness, chemical stability, and high theoretical capacity, which is about two times that of

---

* Corresponding author. Tel.: +86 532 8402 2681; fax: +86 532 8402 3927.
  E-mail address: gjx1213@126.com (J. Guo).

commercial graphite [1–13]. The lithium storage mechanism of SnO$_2$ anode includes two processes: conversion reaction of SnO$_2$ + 4Li$^+$ + 4e$^-$ = Sn + 2Li$_2$O, and alloy reaction of Sn + xLi$^+$ + xe$^-$ = Li$_x$Sn (0 ≤ x ≤ 4.4). Normally, the conversion reaction of SnO$_2$ is believed to be electrochemically irreversible. So the theoretical capacity of SnO$_2$ is generally calculated to be ~780 mAh g$^{-1}$ based on the alloy reaction (4.4 Li per molecular). Unfortunately, the commercialization of SnO$_2$ materials for LIBs anodes is still largely hampered by their large volume changes (~300%) during repeated Li$^+$ insertion/extraction, which results in rapid capacity fading upon extended cycles [14–17]. In the meanwhile, the electron conductivity of SnO$_2$ is poor.

One of the effective solutions to circumvent these obstacles is carbon coating, which not only alleviates the volume changes but also increases the electronic conductivity of the electrode [18–25]. However, carbon coating method still suffers its shortcomings. SnO$_2$ is liable to be reduced at high carbonization temperature [26], and the additional conductive carbon will not only sacrifice the capacity of hybrid composites but also fail to supply residual buffer space to relieve mechanical stress induced during the repeated electrochemical processes [27]. Properly constructing the nanostructured features such as particle sizes, morphologies, and pores has been considered as another valid method to improve the lithium-ion storage performance of SnO$_2$. To date, besides some well-defined hollow nanospheres [28–30] and nanoboxes [31], the one-dimensional (1D) nanostructures (nanotubes, nanorods, and nanowires) of SnO$_2$ are abundantly documented [32–37]. Furthermore, 2D nanosheets are particularly attractive for Li$^+$ storage owing to their unique surface characteristics and structural flexibility, and have received special attention [39–47]. Encouraged by the recent achievements demonstrated about the porous transitional metal oxides for improved Li$^+$ storage properties [48–51], it is highly desirable to rationally design and synthesize the proper 2D porous SnO$_2$ nanostructures, which are intrinsically endowed with the benefits of both the 2D structural flexibility and porous features, to obtain enhanced Li$^+$ storage properties.

In this work, mesoporous SnO$_2$ nanosheets have been successfully synthesized through a so-called evaporation-induced self-assembly (EISA) process followed by thermal treatment. Here, triblock copolymer (HO(CH$_2$CH$_2$O)$_{106}$(CH$_2$CH(CH$_3$)O)$_{70}$(CH$_2$CH$_2$O)$_{106}$H) (F127) is chosen as soft template for the formation of mesopores in the SnO$_2$ nanosheets. Based on the combined structural features of 2D flexible nanosheets and pores with the corresponding high surface area, the as-prepared mesoporous SnO$_2$ nanosheets can not only buffer the volume strain and expansion induced during the repeated Li$^+$ insertion/extraction processes, but also boost the Li$^+$ and electrons transport and increase the contact between the electrolyte and active materials, thus exhibiting enhanced Li$^+$ storage properties when they are tested as anode materials for LIBs.

## 2. Experimental

### 2.1. Sample preparation

All regents are of analytical grade and are used as purchased without further purification. The typical synthesis progress of SnO$_2$ nanosheets is described as shown in Fig. 1. Firstly, 0.02 mol SnCl$_2$·2H$_2$O and 1.42 g F127 are dissolved into 30 mL ethanol. The mixture is refluxed at 100 °C for 8 h to obtain sol. In the next EISA approach, the sol is transferred into a Petri dish and the ethanol is evaporated at room temperature (RT). After about 1 day, a transparent membrane is formed, then it is aged at 50 °C for additional 7–10 days. The resultant gel is loaded into a tube furnace and sintered at 400 °C for 3 h in air to prepare SnO$_2$ nanosheets. The
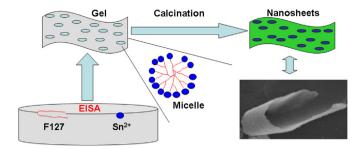


**Fig. 1.** Schematic illustration of the synthesis progress of SnO$_2$ nanosheets.

traditional sol–gel process is utilized to prepare SnO$_2$ nanoparticles for comparison: The sol is aged at 50 °C for 7–10 days in a beaker, followed by calcination at 400 °C.

### 2.2. Materials characterization

The crystallographic information of the samples is measured with powder X-ray diffraction (XRD, Philips X'-pert X-ray diffractometer, Cu Kα radiation: λ = 0.154056 nm). Transmission electron microscope (TEM) analysis is performed using a JEOL, JEM-2100. Scanning electron microscope (SEM) is obtained with a JEOL JSM-7500F scanning electron microscope. N$_2$ adsorption–desorption isotherms of the products are measured at 77 K using Micromeritics Co. Ltd., Tristar. The total specific surface area is determined with the multipoint Braunauer–Emmett–Teller (BET) method.

### 2.3. Electrochemical measurements

The electrochemical tests are carried out with a CR2016-type coin cell. Metallic lithium sheet is used as the negative electrode. The working electrode is fabricated by compressing a mixture of active materials (SnO$_2$ nanosheets or SnO$_2$ nanoparticles), conductive material (acetylene black) and polyvinylidene fluoride (PVDF) in a weight ratio of 75:15:10 onto a copper foil. The typical mass load of active material is about 1–2 mg cm$^{-2}$. The electrode is dried at 120 °C for 24 h in vacuum oven and the cell assembly is operated in a glove box filled with pure argon. The Clegard 2300 microporous film is used as separator. The electrolyte solution is 1 M LiPF$_6$ dissolved in a mixture of ethylene carbonate (EC)/dimethyl carbonate (DMC)/ethyl methyl carbonate (EMC) (1:1:1 in volume) (Zhangjiagang, China). Charge–discharge experiments are performed between 3 and 0.01 V on a LAND CT2001A Battery Cycler (Wuhan, China).

## 3. Results and discussion

Observed in the SEM image (Fig. 2a), SnO$_2$ prepared with traditional sol–gel method consists of agglomerated small grains with rough surface. It can be clearly seen in the TEM image (Fig. 2b) that SnO$_2$ particles are uniform and the typical size is estimated to be 8 ± 2 nm. Fig. 2c shows the SEM image of SnO$_2$ nanosheets, in which two characteristic sheets of flat and curly are observed, indicating the good structural flexibility. With a closer examination (Fig. 2d), the curly nanosheets possess relatively smooth surface and the thickness of several nanometers. The TEM image of SnO$_2$ nanosheets shown in Fig. 2e confirms the smooth surface and reveals the stacked layer-by-layer architectures from the edge of nanosheets. When viewed under higher magnification TEM (Fig. 2f), it can be clearly observed that the nanosheets are composed of compacted small nanoparticles. Moreover, there are
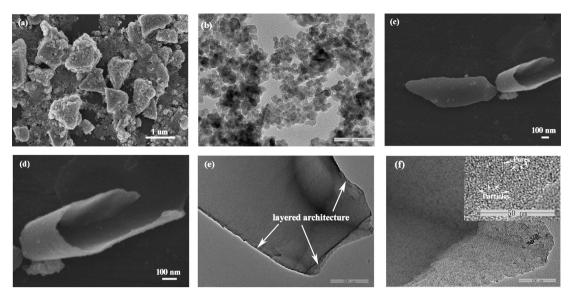
**Fig. 2.** (a) SEM and (b) TEM images of SnO$_2$ nanoparticles, (c, d) SEM and (e, f) TEM images of SnO$_2$ nanosheets. The inset in (f) is the magnified TEM image.

many bright contrasts between the nanoparticles, implying the existence of pores.

The crystal structure of SnO$_2$ nanosheets and nanoparticles is characterized with powder XRD. As is shown in Fig. 3, all the diffraction peaks of the two samples can be assigned to the tetragonal phase SnO$_2$ with space group P42mnm. (JCPDS card no. 41-1445). The absence of peaks corresponding to other phases indicates the high purity of these two samples, and their good crystallization is revealed by the sharp and intense diffraction peaks. There is no distinct difference in peak position and intensity between the SnO$_2$ nanosheets and nanoparticles. The average particle sizes of SnO$_2$ nanosheets and nanoparticles are calculated to be 5.3 and 7.4 nm, respectively, based on the (110) peak intensity with the Scherrer's equation.

With the aim to reveal the porous features and the specific surface area of the SnO$_2$ nanosheets, BET gas-sorption measurements are performed. Fig. 4a and b shows the N$_2$ adsorption−desorption isotherms and its corresponding Barrett−Joyner−Halenda (BJH) calculations for pore-size distribution and pore volume of SnO$_2$ nanosheets, respectively. Fig. 4a exhibits a clear hysteresis loop within the relative pressure ranges of ~0.45−0.75, revealing its mesoporous structure. As shown in Fig. 4b, the BJH pore-size distribution exhibits that most of the
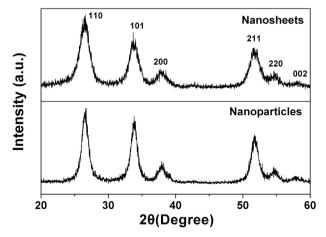
pores are centered at about 4.1 nm. The SnO$_2$ nanosheets possess a high BET surface area of 128.8 m$^2$ g$^{-1}$ and a pore volume of 0.18 cm$^3$ g$^{-1}$. As illustrated in Fig. 1, the formation of mesopores in the SnO$_2$ nanosheets should be attributed to the self-assembly of surfactant molecules [51,52]. In the ethanol evaporation step, the concentration of F127 in the sol increases slowly. Thus the F127 micelles are formed due to the self-assembly of F127 molecules. During the heat-treatment progress, the F127 micelles inside of the dried gel are burned off, and the mesopores are generated in the original positions of micelles.

Inspired by the exciting 2D flexible and mesoporous structures, the Li$^+$ storage properties of the as-synthesized SnO$_2$ nanosheets are investigated with a standard SnO$_2$/Li coin cell. The electrochemical properties of SnO$_2$ nanoparticles are also tested for comparison. Fig. 5a shows the typical charge−discharge voltage profiles of SnO$_2$ nanosheets and nanoparticles in their first cycle at current density of 100 mA g$^{-1}$. These two voltage profiles show the typical features of SnO$_2$ anode with two poorly defined plateaus in the discharge curve. The first plateau at ~0.7 V can be ascribed to the formation of Sn from SnO$_2$. The second one close to 0 V corresponds to the lithium alloying reaction with Sn. And the corresponding de-alloying of Li$_x$Sn can be observed at ~0.6 V plateau of the charge curve.

Fig. 5b compares the cycling performance of SnO$_2$ nanosheets and nanoparticles at 100 mA g$^{-1}$. The data obtained from SnO$_2$ nanoparticles shows a high initial discharge capacity of 935.4 mAh g$^{-1}$, but severe capacity fade occurs in the following 15 cycles leading to a poor reversible capacity of 194.8 mAh g$^{-1}$ after 30 cycles. On the contrary, SnO$_2$ nanosheets deliver excellent cycling stability up to 300 cycles. In the initial cycle, SnO$_2$ nanosheets show high discharge and charge capacities of 1338.6 and 732.5 mAh g$^{-1}$, respectively. The low initial coulombic efficiency of 55% should be assigned to the high surface area of porous 2D features, which will lead to the extra consumption of Li$^+$ during the irreversible formation of solid−electrolyte interface (SEI) layer. After initial several conditioning cycles, the coulombic efficiency rises rapidly and remains over 97% after the 5th cycles, indicating the highly reversible Li$^+$ intercalation/extraction reaction for SnO$_2$ nanosheets. Excellent capacity retention is observed for porous SnO$_2$ nanosheets. A high reversible discharge capacity of 763.2 mAh g$^{-1}$ can be retained even after 300 cycles, demonstrating excellent capacity retention with a capacity fading of 0.08%
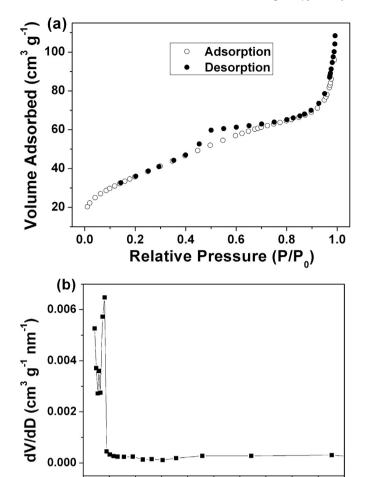


**Fig. 3.** XRD patterns of SnO$_2$ nanosheets and SnO$_2$ nanoparticles.

**Fig. 4.** (a) The N$_2$ adsorption–desorption isotherms and (b) the pore-size distribution of mesoporous SnO$_2$ nanosheets.

charge–discharge progress, the second rate performance test progress, and final high rate (500 mA g$^{-1}$) progress. In the initial cycle, high discharge and charge capacities of 1314.6 and 671.8 mAh g$^{-1}$ are obtained, respectively, with a corresponding coulombic efficiency of 51%. As expected, the unique mesoporous SnO$_2$ nanosheet structures exhibit excellent cycling performance. The reversible discharge capacities retain almost constant and are obtained as high as 553.6 mAh g$^{-1}$ till the 250th cycles. After that, an interesting increase of reversible capacities is observed from the ~250th to the ~400th cycle. The value of discharge capacity increases from ~550 to ~800 mAh g$^{-1}$ during this progress. When the capacities reach stable, the rate performance is tested and detailed results are presented in Fig. 7. After the rigorous rate test (the 450th cycle), the charge–discharge rate turns to high current density of 500 mA g$^{-1}$, and the specific capacities keep stable over 450 mAh g$^{-1}$ till ~1000 cycles, showing outstanding capacity retention. Moreover, the columbic efficiency of porous SnO$_2$ nanosheets increases from the initial ~51%–92% in the second cycle, and remains close to 100% throughout the charge–discharge test after the 5th cycle, suggesting high reversibility of Li$^+$ intercalation/extraction reaction.

The excellent durability of SnO$_2$ nanosheets electrode indicates that the active materials possess a very stable structure, capable of sustaining the volume changes without pulverization and loss of contact from current collector. To examine the structural integrity
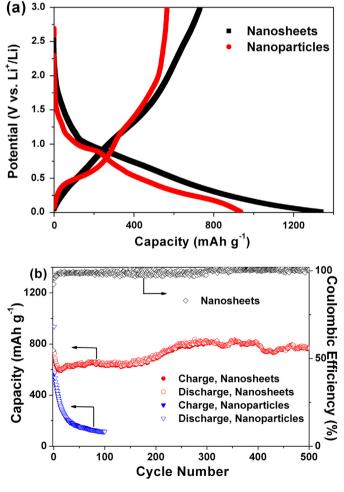


**Fig. 5.** (a) The first charge–discharge profiles of the mesoporous SnO$_2$ nanosheets and SnO$_2$ nanoparticles at 100 mA g$^{-1}$. (b) Cyclic performance of the mesoporous SnO$_2$ nanosheets and SnO$_2$ nanoparticles at 100 mA g$^{-1}$.

per cycle compared with the initial capacity (1338.6 mAh g$^{-1}$). The high reversible capability and outstanding cycling stability of SnO$_2$ nanosheets should be ascribed to their unique 2D mesoporous structures. Interestingly, a gradual increase of reversible capacities for SnO$_2$ nanosheets is observed during about 150–250 cycles, which should be attributed to the specific electrode evolution process of the SnO$_2$ nanosheet. As demonstrated in the literature [53–55], the huge volume Li$_2$O occurred during the first charge cycle will block the further Li$^+$ transfer between electrode and electrolyte, thus suppressing the lithium storage and decreasing the capacity. After a number of cycles, the SnO$_2$ nanosheets become more porous, which can be observed in the subsequent Fig. 6b and c, thereby effectively promoting the electrolyte to access the inner part of the active materials. So the trapped active materials can re-exposure to the electrolyte and release Li$^+$, thus benefiting for the increase of the capacity. And the increased contacting area of active materials with the electrolyte could also result in the improvement of the capacity.

With the aim to evaluate the potential application of the presented porous SnO$_2$ nanosheets, the electrochemical Li$^+$ storage performance is further tested using one cell at variational current densities. Porous SnO$_2$ nanosheets deliver large and stable Li$^+$ storage properties as well as amazing durability of ultralong life over 1000 cycles. As shown in Fig. 6a, the entire test progress can be divided into three parts, including the first low rate (200 mA g$^{-1}$)
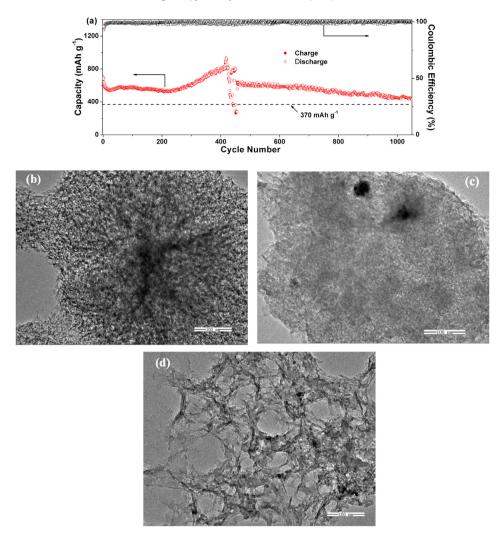
**Fig. 6.** (a) Cyclic performance of the mesoporous $SnO_2$ nanosheets at variational rates up to ultralong cycles over 1000 cycles. (b) TEM images of $SnO_2$ nanosheets after 300 cycles at 100 mA g$^{-1}$. (c) TEM images of $SnO_2$ nanosheets after 300 cycles at 200 mA g$^{-1}$. (d) TEM images of $SnO_2$ nanosheets after 1070 cycles at variational rates.

and reveal the corresponding capacity evolution of the $SnO_2$ nanosheets during repeated electrochemical cycling, three cells including a cell tested after 300 cycles at a rate of 100 mA g$^{-1}$, one cell after 300 cycles at a rate of 200 mA g$^{-1}$, and the cell after 1070 cycles at variational rates are decomposed. The electrode is
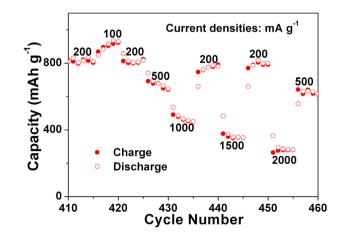


**Fig. 7.** (a) Rate capability of mesoporous $SnO_2$ nanosheets.

observed with TEM. Fig. 6b shows that the porous 2D sheet-like structure is still retained after 300 cycles at 100 mA g$^{-1}$, but the pores become larger compared with the pristine $SnO_2$ nanosheets. According to the literature [38], larger pores are formed from the coalescence of small pores, which could reduce the interfacial surface area between the nanosheets and the electrolyte, thus decreasing the surface energy of the system. As shown in Fig. 6c, the similar result is observed from the TEM image of $SnO_2$ nanosheets electrode after 300 cycles at 200 mA g$^{-1}$. Based on the TEM observations and the corresponding electrochemical performance of cells after 300 cycles at 100 and 200 mA g$^{-1}$, the stable 2D sheet-like structure is the major reason for the outstanding durability of $SnO_2$ nanosheets anode. Fig. 6d shows the TEM image of $SnO_2$ nanosheets after ultralong electrochemical test of 1070 cycles. The surface of the nanosheets becomes textured and big holes can be observed, indicating the peeling off of $SnO_2$ particles. This explains the capacity decrease during the third high rate progress shown in Fig. 6a. It is worth noting that, the sheet-like morphology still can be identified even after the long cycles of rigorous test, further confirming the contribution of 2D structure to the stable cyclability.

Due to the activation process at the initial ~15 cycles of $SnO_2$ nanosheets electrode, the rate performance obtained from a new cell can not reveal their real features. The presented rate capability here is obtained from the cell that has been charge–discharge at

200 mA g$^{-1}$ for 415 cycles. As is shown in Fig. 7, excellent rate performance of SnO$_2$ nanosheets is observed from 100 to 2000 mA g$^{-1}$. The specific capacity always responses immediately to the tuning of current density, which should be assigned to the concentration polarization of Li$^+$ in the SnO$_2$ nanosheets deriving from a diffusion limited process. The specific capacities are about 910, 800, 670, 460, 360, 280 mAh g$^{-1}$ when the cells are cycled at 100, 200, 500, 1000, 1500, 2000 mA g$^{-1}$, respectively. It is worth noting that, the high reversible capacity of ~910 mAh g$^{-1}$ observed at rate of 100 mA g$^{-1}$ exceeds the theoretical capacity of Sn alloy reaction (Sn + $x$Li$^+$ + $xe^-$ = Li$_x$Sn, $0 \leq x \leq 4.4$). This extra value should be attributed to the partly reversible conversion reaction (SnO$_2$ + 4Li$^+$ + 4$e^-$ = Sn + 2Li$_2$O) of porous SnO$_2$ nanosheets [25], suggesting that the unique mesoporous 2D sheets-like structures can promote the Li$^+$ storage performance. Remarkably, the capacity can recover when the rate turns back to the low current density even under such rigorous testing conditions.

Compared with the values recently reported for SnO$_2$ nanosheets [39–44], our presented sample exhibits better electrochemical performance, especially expanding the cycle life from the ordinary 30–50 cycles ever reported to a prolonged lifespan of 1000 cycles. It also shows superior performance compared with the other SnO$_2$ structures [28,31,32,34,36]. Even compared with the SnO$_2$ nanosheets/carbon hybrid composites electrode, the mesoporous SnO$_2$ nanosheets deliver a comparable reversible capacity but better cycling stability [45–47]. The enhanced Li$^+$ storage property can probably be ascribed to the unique mesoporous nanosheets structure. During the extended charge–discharge processes, the pores and void space that exist between smaller nanoparticles in the nanosheets can effectively accommodate the large volume expansion/contraction; in the meantime, the 2D flexible sheets will better maintain their integrity. Moreover, the mesoporous nanosheets with large surface areas and high pore volume can supply large electrolyte-SnO$_2$ contact area, and at the same time offer a short diffusion path allowing efficient Li$^+$/electron transport. To our best knowledge, such ultralong cycling life over 1000 cycles with large and stable Li$^+$ storage properties for pure SnO$_2$ anode materials has not ever been reported before.

## 4. Conclusions

In summary, designed synthesis route of an EISA followed by calcination approach has been successfully developed for the preparation of mesoporous SnO$_2$ nanosheets. Surfactant F127 is chosen as soft template for the formation of mesopores, and EISA technique plays the key role in determining the thin-sheet morphology of the products. The as-synthesized products show flexible 2D sheet-like structure and demonstrate narrow pore-size distribution centered at 4.1 nm, with the corresponding high BET surface area of 128.8 m$^2$ g$^{-1}$ and a pore volume of 0.18 cm$^3$ g$^{-1}$. The specific mesoporous nanosheet structures can not only withstand the volume change and pulverization of SnO$_2$ and preserve the structural integrity, but also shorten the Li$^+$ and electrons diffusion path and increase contact area between active materials and electrolyte. The electrochemical tests have indicated that the mesoporous SnO$_2$ nanosheets can be used as high-performance anode materials for LIBs with amazing lifespan over 1000 cycles as well as large and stable reversible capacity. TEM images of decomposed electrode after electrochemical cycling have been obtained, revealing that the excellent cycling durability of SnO$_2$ nanosheets should be assigned to the combined advantages of 2D stable sheet-like structure and porous features. Moreover, this rational design and synthesis route for the preparation of 2D nanostructures with pores could probably be a versatile approach to promote the electrochemical performance of other metal oxides.

## References

[1] X.W. Lou, C.M. Li, L.A. Archer, Adv. Mater. 21 (2009) 2536–2539.
[2] J. Ren, J. Yang, A. Abouimrane, D. Wang, K. Amine, J. Power Sources 196 (2011) 8701–8705.
[3] L. Ji, Z. Lin, M. Alcoutlabi, X. Zhang, Energy Environ. Sci. 4 (2011) 2682–2699.
[4] X. Zhu, Y. Zhu, S. Murali, M.D. Stoller, R.S. Ruoff, J. Power Sources 196 (2011) 6473–6477.
[5] B. Zhao, G. Zhang, J. Song, Y. Jiang, H. Zhuang, P. Liu, T. Fang, Electrochim. Acta 56 (2011) 7340–7346.
[6] C. Xu, J. Sun, L. Gao, J. Mater. Chem. 22 (2012) 975–979.
[7] W. Xia, Y. Wang, Y. Luo, J. Li, Y. Fang, L. Gu, J. Peng, J. Sha, J. Power Sources 217 (2012) 351–357.
[8] S.K. Park, S.H. Yu, N. Pinna, S. Woo, B. Jang, Y.H. Chung, Y.H. Cho, Y.E. Sung, Y. Piao, J. Mater. Chem. 22 (2012) 2520–2525.
[9] X. Wang, X. Cao, L. Bourgeois, H. Guan, S. Chen, Y. Zhong, D.M. Tang, H. Li, T. Zhai, L. Li, Y. Bando, D. Golberg, Adv. Funct. Mater. 22 (2012) 2682–2690.
[10] Y. Fang, B. Luo, Y. Jia, X. Li, B. Wang, Q. Song, F. Kang, L. Zhi, Adv. Mater. 24 (2012) 6348–6355.
[11] L. Wang, D. Wang, Z. Dong, F. Zhang, J. Jin, Nano Lett. 13 (2013) 1711–1716.
[12] J. Lin, Z. Peng, C. Xiang, G. Ruan, Z. Yan, D. Natelson, J.M. Tour, ACS Nano 7 (2013) 6001–6006.
[13] J. Deng, C. Yan, L. Yang, S. Baunack, S. Oswald, H. Wendrock, Y. Mei, O.G. Schmidt, ACS Nano 7 (2013) 6948–6954.
[14] D. Deng, J.Y. Lee, Chem. Mater. 20 (2008) 1841–1846.
[15] J.Y. Huang, L. Zhong, C.M. Wang, J.P. Sullivan, W. Xu, L.Q. Zhang, S.X. Mao, N.S. Hudak, X.H. Liu, A. Subramanian, H. Fan, L. Qi, A. Kushima, J. Li, Science 330 (2010) 1515–1520.
[16] L. Cui, J. Shen, F. Cheng, Z. Tao, J. Chen, J. Power Sources 196 (2011) 2195–2201.
[17] C.M. Wang, W. Xu, J. Liu, J.G. Zhang, L.V. Saraf, B.W. Arey, D. Choi, Z.G. Yang, J. Xiao, S. Thevuthasan, D.R. Baer, Nano Lett. 11 (2011) 1874–1880.
[18] L.S. Zhang, L.Y. Jiang, H.J. Yan, W.D. Wang, W. Wang, W.G. Song, Y.G. Guo, L.J. Wan, J. Mater. Chem. 20 (2010) 5462–5467.
[19] D. Ahn, X. Xiao, Y. Li, A.K. Sachdev, H.W. Park, A. Yu, Z. Chen, J. Power Sources 212 (2012) 66–72.
[20] Y. Zhao, J. Li, N. Wang, C. Wu, G. Dong, L. Guan, J. Phys. Chem. C 116 (2012) 18612–18617.
[21] F. Han, W.C. Li, M.R. Li, A.H. Lu, J. Mater. Chem. 22 (2012) 9645–9651.
[22] S. Yang, W. Yue, J. Zhu, Y. Ren, X. Yang, Adv. Funct. Mater. 23 (2013) 3570–3576.
[23] S.J.R. Prabakar, Y.H. Hwang, E.G. Bae, S. Shim, D. Kim, M.S. Lah, K.S. Sohn, M. Pyo, Adv. Mater. 25 (2013) 3307–3312.
[24] X. Zhou, L.J. Wan, Y.G. Guo, Adv. Mater. 25 (2013) 2152–2157.
[25] J. Guo, L. Chen, G. Wang, X. Zhang, F. Li, J. Power Sources 246 (2014) 862–867.
[26] J. Lee, S. Jin, Y. Hwang, J.G. Park, H.M. Park, T. Hyeon, Carbon 43 (2005) 2536–2543.
[27] E. Kang, Y.S. Jung, A.S. Cavanagh, G.H. Kim, S.M. George, A.D. Dillon, J.K. Kim, J. Lee, Adv. Funct. Mater. 21 (2011) 2430–2438.
[28] X.W. Lou, Y. Wang, C. Yuan, J.Y. Lee, L.A. Archer, Adv. Mater. 18 (2006) 2325–2329.
[29] X. Zhou, Y.X. Yin, L.J. Wan, Y.G. Guo, J. Mater. Chem. 22 (2012) 17456–17459.
[30] Y.J. Hong, M.Y. Son, Y.C. Kang, Adv. Mater. 25 (2013) 2279–2283.
[31] Z. Wang, D. Luan, F.Y.C. Boey, X.W. Lou, J. Am. Chem. Soc. 133 (2011) 4738–4741.
[32] Y. Wang, J.Y. Lee, H.C. Zeng, Chem. Mater. 17 (2005) 3899–3903.
[33] Y. Wang, H.C. Zeng, J.Y. Lee, Adv. Mater. 18 (2006) 645–649.
[34] M.S. Park, G.X. Wang, Y.M. Kang, D. Wexler, S.X. Dou, H.K. Liu, Angew. Chem. Int. Ed. 46 (2007) 750–753.
[35] P. Meduri, C. Pendyala, V. Kumar, G.U. Sumanasekera, M.K. Sunkara, Nano Lett. 9 (2009) 612–616.
[36] J. Ye, H. Zhang, R. Yang, X. Li, L. Qi, Samll 6 (2010) 296–306.
[37] S. Chen, M. Wang, J. Ye, J. Cai, Y. Ma, H. Zhou, L. Qi, Nano Res. 6 (2013) 243–252.
[38] T. Kennedy, E. Mullane, H. Geaney, M. Osiak, C. O'Dwyer, K.M. Ryan, Nano Lett. 14 (2014) 716–723.
[39] J.S. Chen, C.M. Li, W.W. Zhou, Q.Y. Yan, L.A. Archer, X.W. Lou, Nanoscale 1 (2009) 280–285.
[40] C. Wang, Y. Zhou, M. Ge, X. Xu, Z. Zhang, J.Z. Jiang, J. Am. Chem. Soc. 132 (2010) 46–47.
[41] X.M. Yin, C.C. Li, M. Zhang, Q.Y. Hao, S. Liu, L.B. Chen, T.H. Wang, J. Phys. Chem. C 114 (2010) 8084–8088.

[42] H.B. Wu, J.S. Chen, X.W. Lou, H.H. Hng, J. Phys. Chem. C 115 (2011) 24605—24610.
[43] J.S. Chen, M.F. Ng, H.B. Wu, L. Zhang, X.W. Lou, CrystEngComm 14 (2012) 5133—5136.
[44] C. Wang, G. Du, K. Ståhl, H. Huang, Y. Zhong, J.Z. Jiang, J. Phys. Chem. C 116 (2012) 4000—4011.
[45] S. Ding, D. Luan, F.Y.C. Boey, J.S. Chen, X.W. Lou, Chem. Commun. 47 (2011) 7155—7157.
[46] S. Ding, J.S. Chen, X.W. Lou, Adv. Funct. Mater. 21 (2011) 4120—4125.
[47] Q. Tian, Z. Zhang, J. Chen, L. Yang, S.I. Hirano, J. Power Sources 246 (2014) 587—595.
[48] J.Y. Luo, J.J. Zhang, Y.Y. Xia, Chem. Mater. 18 (2006) 5618—5623.
[49] K.M. Shaju, F. Jiao, A. Debart, P.G. Bruce, Phys. Chem. Chem. Phys. 9 (2007) 1837—1842.
[50] L. Yu, H.B. Wu, X.W. Lou, Adv. Mater. 25 (2013) 2296—2300.
[51] A. Vu, Y.Q. Qian, A. Stein, Adv. Energy Mater. 2 (2012) 1056—1085.
[52] Q. Sun, X.Q. Zhang, F. Han, W.C. Li, A.H. Lu, J. Mater. Chem. 22 (2012) 17049—17054.
[53] M. Ebner, F. Marone, M. Stampanoni, V. Wood, Science 342 (2013) 716—720.
[54] G. Yang, H. Cui, G. Yang, C. Wang, ACS Nano 8 (2014) 4474—4487.
[55] W. Ai, L. Xie, Z. Du, Z. Zeng, J. Liu, H. Zhang, Y. Huang, W. Huang, T. Yu, Sci. Rep. 3 (2014) 2341.